Journal of Alloys and Compounds 681 (2016) 253–259

Contents lists available at ScienceDirect

Journal of Alloys and Compounds

journal homepage: http://www.elsevier.com/locate/jalcom

Insights into MoS_2-coated $LiVPO_4F$ for lithium ion batteries: A first-principles investigation

Xiaojun Lv [a], Zhenming Xu [a], Jie Li [a, *], Jiangan Chen [b], Qingsheng Liu [c]

[a] School of Metallurgy and Environment, Central South University, Changsha 410083, China
[b] Faculty of Resource and Environmental Engineering, Jiangxi University of Science and Technology, Ganzhou 341000, China
[c] Faculty of Metallurgical and Chemical Engineering, Jiangxi University of Science and Technology, Ganzhou 341000, China

ARTICLE INFO

Article history:
Received 17 January 2016
Received in revised form
22 April 2016
Accepted 23 April 2016
Available online 25 April 2016

Keywords:
First-principles calculations
$LiVPO_4F$
MoS_2 coating
Electron conductivity

ABSTRACT

The structure, stability and electron conductivity of $LiVPO_4F$ covered by MoS_2 were investigated by a first-principles method based on density functional theory. Calculations show that the low-index $LiVPO_4F$ (010) surface exposing Li and O atoms is the lowest energy surface. The formation of a new surface-state near the Fermi level reduces the band gap of the $LiVPO_4F$ surface compared to that of the bulk. For clean $LiVPO_4F$ surfaces, the quantum state near the Fermi level is dominated by the V-3*d* orbital. In addition, PDOS of V atoms shows significant differences in different atomic layers. MoS_2 coating dramatically increases the stability of the $LiVPO_4F$ surface by forming strong covalent bonds with this surface. Additionally, it also enhances the electronic conductivity by reducing the band gap and generating new electronic states at the Fermi level. These theoretical results are consistent with experimental data.

1. Introduction

Lithium ion batteries have been widely applied in the field of portable energy storage because of their advantages of high voltage, high energy density, long cycle life and environmental friendliness [1–5]. Choosing the appropriate electrode materials is a key factor in the production of high-performance lithium ion batteries. The $LiMO_2$ family (M = Co, Mn and Ni) is currently the dominant class of commercial cathode materials for lithium ion batteries [1,6–9]. To overcome the shortage of $LiMO_2$ (M = Co, Mn and Ni), much effort has been directed towards the search for new cathode and anode materials with advantages of higher energy density, longer cycle life, and lower cost [10–19]. Among cathode materials, a series of $LiVPO_4F$ materials have become the promising candidates for next-generation lithium ion batteries [14,17–20]. Compared to the corresponding oxide systems, the phosphate series $LiVPO_4F$ materials generate a higher voltage of 4.2 V and have higher energy density, better thermodynamic stability and better electrochemical properties; additionally, the partial substitution of oxide ions by fluorophosphates ions results in improved three-dimensional structural stability. Barker et al. reported the first synthesis of $LiVPO_4F$ materials by means of CTR (carbothermal reduction), with a specific capacity of 135 and 115 mAh g^{-1} for charge and discharge, respectively, a Coulombic efficiency of 84% and a stable discharge platform of 4.17 V [17–20].

To further improve the capacity and conductivity of $LiVPO_4F$, many recent studies have focused on surface coating of $LiVPO_4F$ by copper [21], conducting polyaniline [22], carbon [23–27] and graphene [28–30]; experimental results show that such coating can reduce polarization and increase electrochemical properties such as cyclability and electric capacity. However, there has been no theoretical study of the surface properties of $LiVPO_4F$ and $LiVPO_4F$-coated materials. To the best of our knowledge, theoretical calculations have only been performed in order to study the bulk and surface properties of $LiFePO_4$. Zhang et al. have studied the electronic structure of $LiFePO_4$ (010) surfaces with adsorbed carbon, by first-principles methods [31]. Ouyang et al. have studied the stability and electronic structure of the (001), (010) and (100) surfaces of $LiFePO_4$ [32]. Wang et al. have pointed that the (010) and (201) surfaces of $LiFePO_4$ exhibit the lowest energies [33]. However, there have been no such theoretical studies on coated $LiVPO_4F$; thus, there is currently only a superficial understanding of the influence of coating material on the surface stability of $LiVPO_4F$.

More recently, large-area 2D MoS_2 has been synthesized experimentally [34–36] and has attracted increasing attention due

* Corresponding author.
E-mail address: 15216105346@163.com (J. Li).

http://dx.doi.org/10.1016/j.jallcom.2016.04.240
0925-8388/

to its unique physical, optical and electrical properties, which are correlated with its 2D ultrathin atomic layer structure [37–41]. Therefore, we proposed MoS_2 coating on $LiVPO_4F$ surfaces. To explain our experimental results, we report first-principles calculations and a systematic investigation of the structure, stability and electron conductivity of MoS_2-coated $LiVPO_4F$ materials.

2. Calculation methodology and models

In this work, all calculations were performed using density functional theory (DFT) with the exchange-correlation functional treated in spin-polarized GGA [42], as implemented in the CASTEP package [43]. Ultrasoft pseudo potentials (USPP) introduced by Vanderbilt [44] have been employed for all ion-electron interactions. The energy convergence criterion for self-consistent field (SCF) calculations was 1×10^{-6} eV/atom. Convergence was tested with respect to values of energy cutoff as well as *k*-point mesh. Based on the convergence test, an energy cutoff of 340 eV was chosen in order to ensure that total energies were converged within 1×10^{-4} eV/cell. Brillouin zone sampling of the bulk material was carried out with a $6 \times 6 \times 4$ *k*-points mesh using the method of Monkhorst–Pack [45]. The DFT + U method was adopted, and a Hubbard-like correlation was added in order to account for the strong correlation among *d* electrons of vanadium ions, using the reported value of U = 3 eV for vanadium compounds [15,16,46].

Tests with different thicknesses of vacuum regions showed that a vacuum region with 20 Å thickness on the chapped surface is good enough to fairly represent bulk materials. The surface energy calculations reported here were performed using a (1×1) slab structure, where periodicity was maintained in the direction parallel to surface atoms. In all surface calculations, the use of symmetry in bulk crystals resulted in failed calculations, and the *k*-point mesh was cut down to a single *k*-point in the direction perpendicular to the surface plane. Conversely, the *k* grid in the direction parallel to surface atoms was used for bulk calculations [47]. For surface-slab cell units of the same stoichiometry, a study of the effect of height on energy of surface layers [48] indicates that when the intercept depth is more than 9.897 Å, the difference in surface energy is negligible for (100), (010), (001), (110), (101), (011), (111), (201) and (301) surfaces. Therefore, slab thicknesses of more than 9.897 Å combined with relaxation of outer atoms can yield converged surface energies for the above nine surfaces in view of the precision and efficiency of computations. In this work, slab calculations were carried out for (100), (010) and (001) $LiVPO_4F$ surfaces. The outer six atom layers (e.g., layers 1–6 of the (010) surface in Fig. 1(a)) were allowed to move, while the remaining internal layers were frozen in bulk positions to simulate the bulk properties of this material. In addition, all atomic layers were permitted to relax in the remaining surface calculations.

Surface energy is approximatively equal to the corresponding cleavage energy [49]. When a crystal is cleaved, two terminated surfaces with equally unrelaxed slab energies are created simultaneously. Therefore, the cleavage energies, E_C, can be obtained from the total energies of the unrelaxed slabs through the following equation: $E_C = (E_{slab}^{unrel}(a) + E_{slab}^{unrel}(i) - xE_{Bulk})/2S$, where $E_{slab}^{unrel}(a)$ and $E_{slab}^{unrel}(i)$ are the energies of the unrelaxed slab (a) and its complementary slab (i), respectively [32,50]. E_{Bulk} is the energy per unit cell, x is the total number of unit cells in two slabs, 2 is the total number of surfaces created upon cleavage and S is the corresponding surface area.

3. Results and discussion

3.1. Surface stability

The stability of the surface system depends not only on the crystal direction but also on the exposed atoms, and the adsorption process usually occurs only on the surface, which is most stable to cleaving [31]. To locate the lowest energy surface of $LiVPO_4F$, the surface energy was first calculated for nine surfaces: (100), (010), (001), (110), (101), (011), (111), (201) and (301), all having Li and O atoms exposed to the vacuum [33]. The calculated surface energies of multiple directions for $LiVPO_4F$ (100), (010), (001), (110), (101), (011), (111), (201) and (301) surfaces exposing Li and O atoms are listed in Table 1. It can be seen that different crystal face directions show large differences in surface energy. Among all of these calculated surfaces, (201) has the highest surface energy of 0.608 J/m^2. Conversely, the Li (O)-terminated (010) surface has the lowest surface energy of 0.216 J/m^2, and this is similar to the lowest energy surface (010) of $LiFePO_4$ as reported by Wang. L [33].

Based on the lowest energy surface (010), surface energies of 16 configurations exposing different atoms were obtained, which are also listed in Table 1. The results in Table 1 show that there are eight pairs of surface structures having the same surface energy, such as F(V)-terminated (010) and Li(O)-terminated (010). This is because the same number of broken bonds is generated by cleaving a bulk $LiFePO_4$. When the (010) surface is terminated with O(O) atoms or P(V) atoms, the corresponding surface energy is the highest at 1.031 J/m^2; this is because more energy is needed to break the strong covalent P–O and V–O bonds. If the (010) surface is cut through (0, 0, 0) and (0, 0.5, 0), Li and O atoms are exposed at the outer surface and this configuration has the lowest surface energy. We can conclude that the low-index (010) surface, exposing Li and O atoms, is the most stable and dominant. These results indicate that the Li(O)-terminated (010) surface is most likely to be exposed to the environment. Therefore, the following MoS_2 adsorption calculations were performed on this most stable Li (O)-terminated (010) surface.

3.2. Surface relaxation of $LiVPO_4F$ (010)

Before carrying out adsorption calculations, the clean $LiVPO_4F$ (010) surface model was fully relaxed by optimizing the fractional coordinates, and the equilibrium configuration is shown in Fig. 1a. For the outermost layer, Li-2*i*, P-2*i* and O-2*i* sites all move upward in the Y direction while V-1*a* also moves upward. It is found that the Li-2*i* atom undergoes the greatest upward relaxation by 0.06 Å. This indicates the enrichment of Li atoms on the $LiVPO_4F$ (010) surface, which is consistent with the preceding conclusion in Section 3.1 that the (010) surface exposing Li and O atoms has the lowest surface energy. Therefore, the relaxation effect is notable for surface atoms in the (0 1 0) surface of $LiVPO_4F$.

The band structures of bulk $LiVPO_4F$ and its (0 1 0) surface near the Fermi level, are shown in Fig. 2a and b, respectively. From Fig. 2b, the band gap of the $LiVPO_4F$ (0 1 0) surface is found to be 0.149 eV, which is significantly smaller than the bulk band gap of 1.635 eV. The $LiVPO_4F$ (0 1 0) surface creates five V–O(F) bonds, while V atoms in the bulk form six V–O(F) bonds. The breakage of V–O(F) bonds at the (010) surface enhances the activity of V atoms and results in a significant increase of the electron number in the V-3*d* orbitals. Accordingly, several new bands are formed at the top of the valence band and at the bottom of the conduction band for the (010) surface of $LiVPO_4F$, or the so-called surface state, resulting in a narrowed band gap. It is well-known that band gaps calculated by first principles are significantly underestimated. In this work, the only relevant numbers are the differences between the band gaps

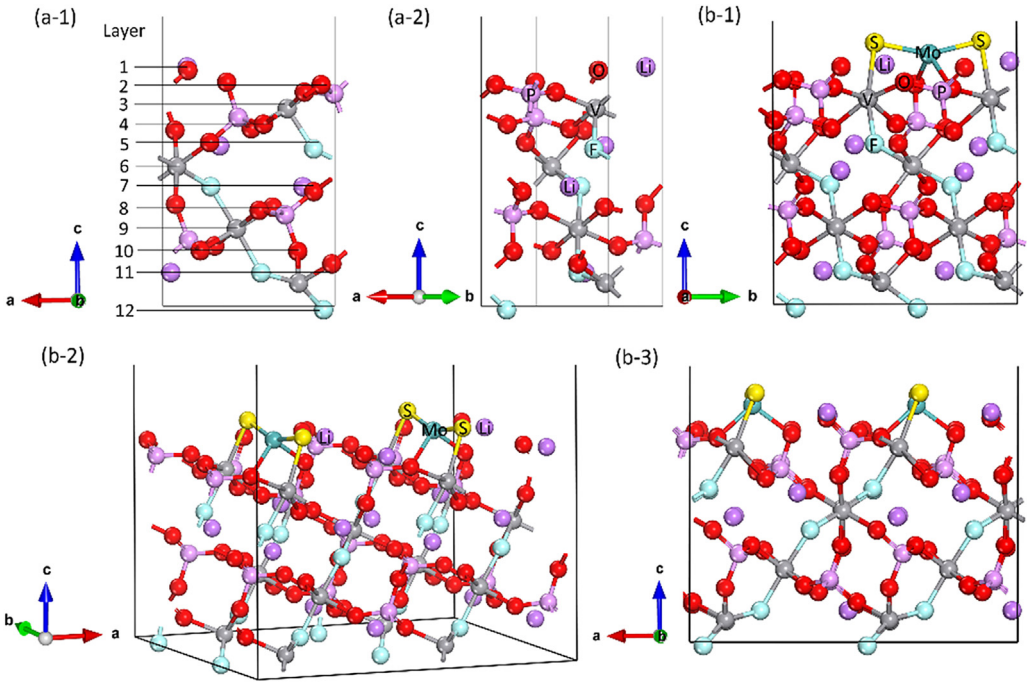

Fig. 1. Structural diagram of the $LiVPO_4F$ (010) surface exposing Li and O atoms (a) relaxed (1 × 1) clean surface; (b) relaxed (2 × 2) supercell covered by MoS_2.

Table 1
Calculated surface energies (J/m^2) for multiple directions and terminations of $LiVPO_4F$ surfaces.

Surface (Li (O)-terminated)	E_S (J/m^2)	Atom terminated (010)	E_S (J/m^2)	Atom terminated (010)	E_S (J/m^2)
(100)	0.523	V(F)	0.332	V(P)	0.585
(010)	0.216	F(V)	0.216	P(V)	1.031
(001)	0.490	Li(F)	0.397	O(P)	0.692
(110)	0.363	O(Li)	0.328	O(P)	0.423
(101)	0.268	O(O)	0.423	O(O)	0.328
(011)	0.439	O(O)	0.692	O(O)	0.397
(111)	0.397	O(O)	1.031	Li(O)	0.216
(201)	0.608	P(O)	0.585	F(Li)	0.332
(301)	0.461				

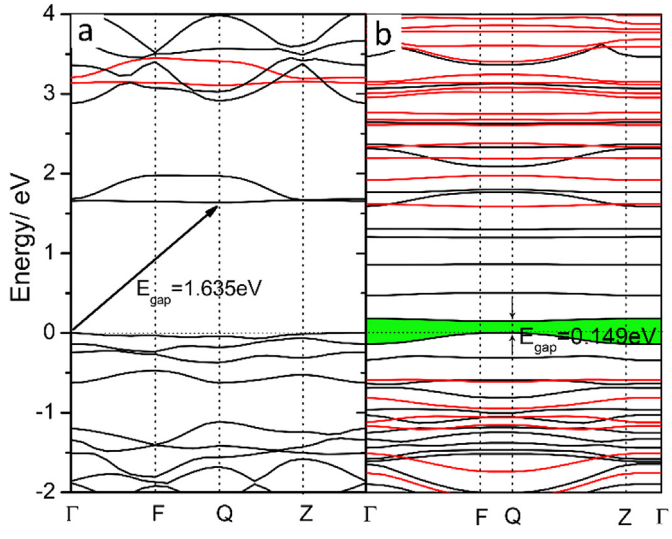

Fig. 2. Band structure of bulk $LiVPO_4F$ (a) and $LiVPO_4F$ (0 1 0) surface (b) near the Fermi level.

of the clean surface and those with adsorbate MoS_2. Therefore, the absolute band gap is not important, and the underestimation of gaps by GGA can be ignored. Fig. 3a shows the total density of states (DOS) of all layers and detached layers (top, middle and bottom) of the $LiVPO_4F$ (010) surface. At first glance, total DOS distribution of spin-up and spin-down states is the distinguishing factor above −1 eV. This is a reflection of the ferromagnetic phase structure. The quantum state near the Fermi level is dominated by the V-3*d* orbital. In addition, PDOS of the V atom vary greatly at different atomic layers (layer 3, 6 and 9 in Fig. 1(a)). DOS of the top layers near the Fermi level show that V-3*d* spin-down state determines the electron transmission properties. In the middle region of atomic layers, the electronic state near the Fermi level is dominated by the V-3*d* spin-up state. Finally, in the bottom region of atomic layers, representing the bulk material, the V-3*d* spin-down state again predominantly composes the electronic state near the Fermi level. These results indicate that the surface region is dramatically different from the bulk, not only in geometry but also in electronic structure. The band gap narrowing due to newly created bands, facilitates the transfer of electrons from the valence band to the conduction band through the forbidden band. Therefore, smaller particles of $LiVPO_4F$ materials result in dramatically enhanced electrochemical properties because of improvements in electron transmission.

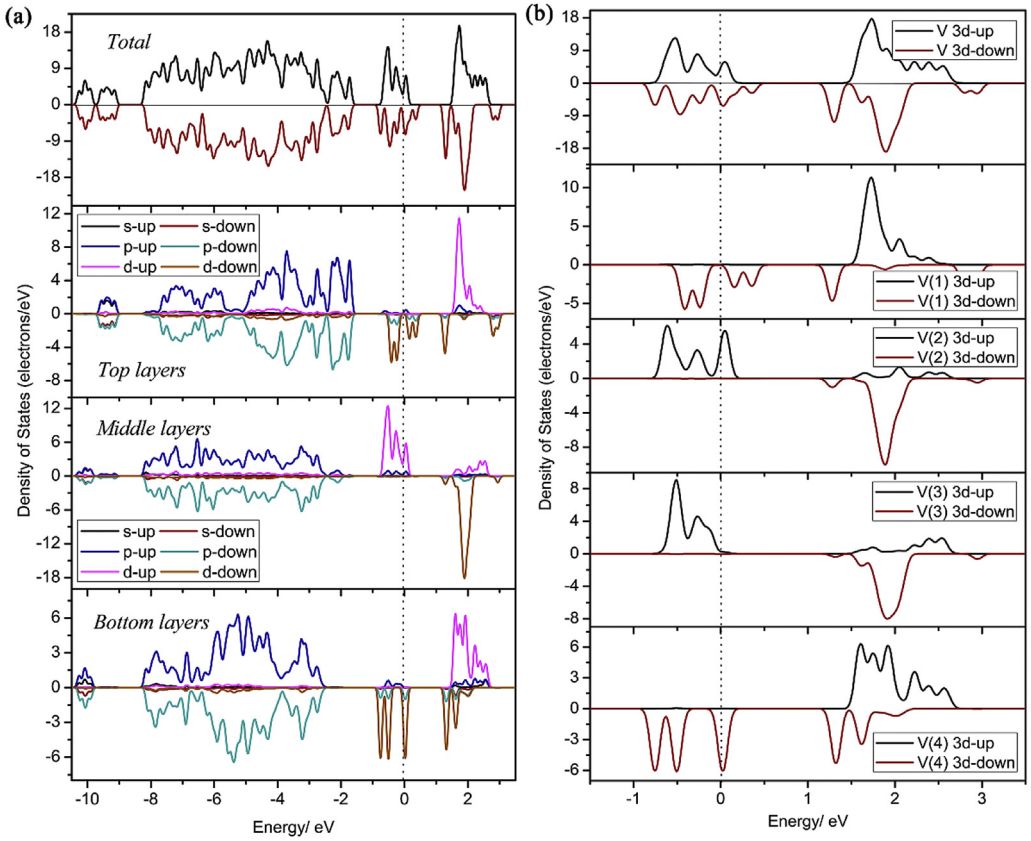

Fig. 3. PDOS of total, top, middle, and bottom layers (a) and V atom in different layers (b).

3.3. $LiVPO_4F$ (010) surface covered by MoS_2

A (2 × 2) supercell model was adopted to simulate the high concentration of adsorbate MoS_2 on the $LiVPO_4F$ (010) surface. In a theoretical study of carbon-coated $LiFePO_4$ [31], a model of a single carbon atom adsorbed on the $LiFePO_4$ surface cell was adopted to calculate the electronic structure; however, the experimental SEM and TEM of carbon-coated $LiFePO_4$ show a carbon network structure [51–55]. The calculations in the present work provide a qualitative way for determining the mechanism of enhanced electron transmission. SEM results (Fig. 4) indicate that MoS_2 not only coats the $LiVPO_4F$ surface but also forms contacts with itself to form a 3D network structure. Therefore, the present work employs an adsorption model of two MoS_2 molecules coating the surface of $LiVPO_4F$ electrode, in the interest of simplicity of calculation and preservation of accuracy. The $LiVPO_4F$ (010) surface covered by MoS_2, after relaxation, is shown in Fig. 1b. It can be seen that in the equilibrium adsorption configuration, the Mo atom bonds with the bare O atom of the PO_4 tetrahedron and the bridge O atom between V and P atoms. Additionally, two S atoms bond with the two bare V atoms, which are not saturated due to the breakages of V–F bonds from the clean $LiVPO_4F$ (010) surface. Compared to bulk MoS_2, the Mo–S bond in the adsorbate MoS_2 is equivalent to that in bulk (2.39 Å), while the S–Mo–S bond angle of 155° is significantly different from that of 81° in the bulk. These structural changes in adsorbate MoS_2 demonstrate that the interface of the MoS_2 layer coating the $LiVPO_4F$ (010) surface is corrugated because the surface is flat in bulk MoS_2.

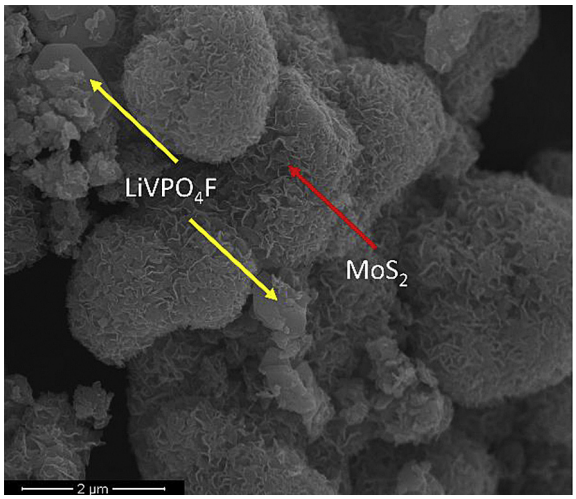

Fig. 4. SEM of MoS_2 coated $LiVPO_4F$ surface. Flat zone is $LiVPO_4F$, and folded zones correspond to MoS_2.

Surface adsorption energy (E_a) is defined as follows: $E_a = E(MoS_2) + E(\text{clean surface}) - E(\text{surface with } MoS_2)$. Therefore, the surface adsorption energy for the $LiVPO_4F/MoS_2$ system depicted in Fig. 1b is 17.34 eV/supercell, which represents the high stability of the MoS_2 surface coating on the $LiVPO_4F$ (010). This indicates that the adsorption process is exothermic and spontaneous. The great advantage of MoS_2-coating on the $LiVPO_4F$ (010) surface is that MoS_2 can significantly reduce the activity of Li-terminated surfaces due to the saturation effect of bare V atoms on the $LiVPO_4F$ surface. As seen in Fig. 5, there is a substantial rearrangement of electron density due to strong covalent interactions between the adsorbate and substrate (as Mo–O and V–S

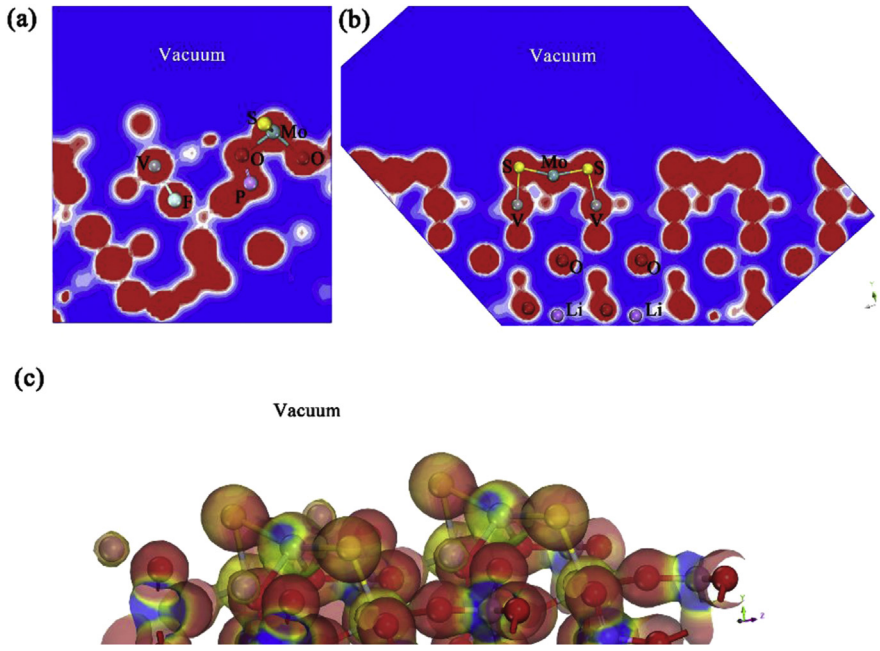

Fig. 5. Electron density of $LiVPO_4F$ (010) surface covered by MoS_2 molecule (a) (−0.5 0.8 0) section; (b) (100) section; (c) 3D isosurface.

bonds), which may be the reason for the increased stability of the $LiVPO_4F$ (010) surface. These strong covalent bonds also confirm the larger binding energy 17.34 eV of the MoS_2 coating on the $LiVPO_4F$ (010) surface. These results suggest that the atoms in the adsorbed MoS_2 molecules bond with the $LiVPO_4F$ surface through chemisorption.

Fig. 6a shows the total density of states (DOS) of the $LiVPO_4F$ (010) surface with two adsorbed MoS_2 molecules. At first sight, the spin-up and spin-down distributions of all electronic states are consistent, which reflects the antiferromagnetic phase structure. It can be concluded that the adsorbate MoS_2 changes the magnetic structure of the $LiVPO_4F$ (010) surface system. Fig. 6b shows that the quantum state near the Fermi level is dominated by the V-3*d* state, which determines the extent of electron transfer. Additionally, the Mo-3*d* state also contributes to the quantum state near the Fermi level. These new electronic states at the Fermi level dramatically improve the ability of electrons to hop from the valence band to the conduction band because the electronic conductivity of $LiVPO_4F$ (010) surface-coated with MoS_2 is proportional to the density of electronic states near the Fermi level. The increase of surface conductivity is beneficial to the performance of Li-ion batteries in normal conditions.

These results indicate that on one hand, the extent of electron transfer is enhanced as a result of the reduction of the band gap and the creation of new electronic states at the Fermi level compared to those of the bulk and clean surface. On the other hand, MoS_2 can significantly decrease the activity of $LiVPO_4F$ surface. These theoretical results are consistent with the experimental results.

Based on the experimental and theoretical results, three main factors clearly contribute to the improved electrochemical performance of MoS_2-coated $LiVPO_4F$. First, based on crystal chemistry theory, smaller particle sizes have a larger specific area and thus, a high surface energy. The resulting thermodynamically unsteady state favours the process of film formation. Therefore, MoS_2 added during the synthesis of $LiVPO_4F$ can observably improve the stability of the particle surface. In addition, the MoS_2 coating can form a network structure on the $LiVPO_4F$ surface, strengthening the inter-particle contacts. Further, the band gap of (010) surfaces,

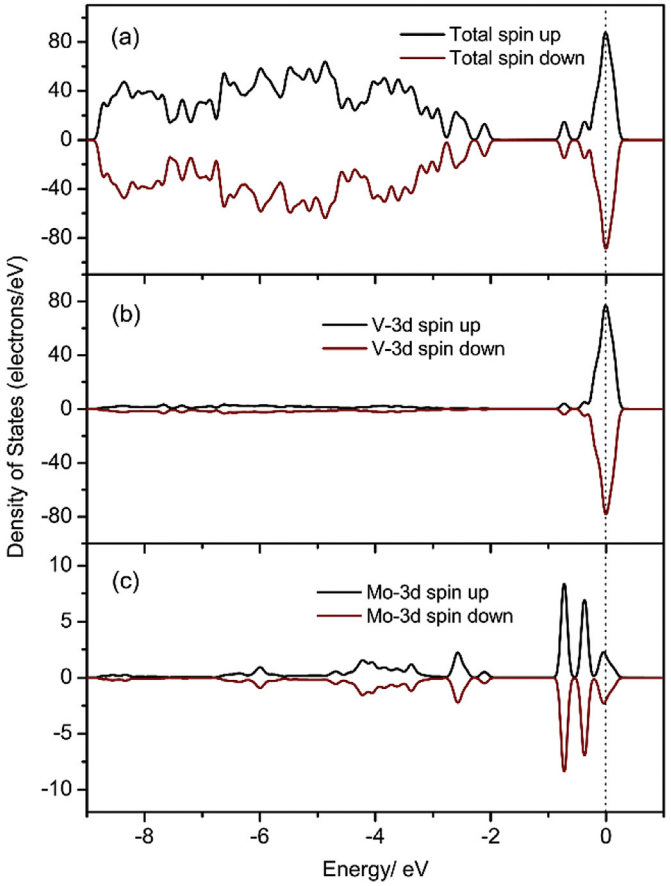

Fig. 6. Total density of states of $LiVPO_4F$ (010) surface covered by MoS_2 (a) and PDOS of V-3*d* (b) and Mo-3*d* (c) atom.

irrespective of whether they are coated with MoS_2, is far lower than that of the bulk (as shown in Fig. 2). The combination of these

conditions results in a better electron transmission channel, reduces the polarization, and improves the reversibility of the charge-discharge processes [56]. Second, the MoS_2-coating partially inhibits secondary crystalline growth of $LiVPO_4F$ particles, thereby diminishing the crystal size and increasing the specific surface area [57,58]. This shortens the path for embedding Li^+ and thus favours Li ion migration. Finally, and most importantly, the MoS_2-coating dramatically improves the electron conductivity of $LiVPO_4F$ particles, reducing the impedance of electrode system.

4. Conclusions

The structure, stability and electronic structure of $LiVPO_4F$ covered by MoS_2 were studied by a first-principles method based on DFT. The following conclusions are drawn based on the calculations:

a) The low-index $LiVPO_4F$ (010) surface exposing Li and O atoms is the most stable and dominant and thus favours the diffusion of Li ion.
b) The formation of new surface states near the Fermi level narrows the band gap of the $LiVPO_4F$ (010) surface compared to the bulk. In a clean $LiVPO_4F$ surface, the quantum state near the Fermi level is dominated by the V-3*d* state. Further, PDOS of V atoms vary significantly in different atomic layers.
c) In MoS_2-coated $LiVPO_4F$ surfaces, the quantum state near the Fermi level is dominated by the V-3*d* state hybridized with the Mo-3*d* state. The MoS_2-coating on the $LiVPO_4F$ surface significantly decreases the activity of the $LiVPO_4F$ surface by forming strong covalent bonds. In addition, it enhances the electron conductivity by reducing the band gap and generating new electronic states at the Fermi level. These theoretical results are consistent with the experimentally measured performance.

Acknowledgements

We sincerely acknowledge the High-Performance Computing Center of CSU, China. This work was financially supported by the National Science and Technology Support Project of China (No. 2012BAE08B02) and the National Natural Science Foundation of China (No.51264011).

Appendix A. Supplementary data

Supplementary data related to this article can be found at http://dx.doi.org/10.1016/j.jallcom.2016.04.240.

References

[1] E. Castel, E.J. Berg, M. El Kazzi, P. Novák, C. Villevieille, Differential electrochemical mass spectrometry Study of the interface of $xLi_2MnO_3\cdot(1-x)LiMO_2$(M = Ni, Co, and Mn) material as a positive electrode in Li-ion batteries, Chem. Mater. 26 (2014) 5051–5057.
[2] D. Mikhailova, A. Sarapulova, A. Voss, A. Thomas, S. Oswald, W. Gruner, D.M. Trots, N.N. Bramnik, H. Ehrenberg, $Li_3V(MoO_4)_3$: a new material for both Li extraction and insertion, Chem. Mater. 22 (2010) 3165–3173.
[3] D. Ai, K. Liu, Z. Lu, M. Zou, D. Zeng, J. Ma, Aluminothermal synthesis and characterization of $Li_3V_{2-x}Al_x(PO_4)_3$ cathode materials for lithium ion batteries, Electrochim. Acta 56 (2011) 2823–2827.
[4] M.S. Whittingham, Lithium batteries and cathode materials, Chem. Rev. 104 (2004) 4271–4301.
[5] Z. Xu, X. Lv, J. Li, J. Chen, Q. Liu, A promising anode material for sodium-ion battery with high capacity and high diffusion ability: graphyne and graphdiyne, RSC Adv. 6 (2016) 25594–25600.
[6] Y. Koyama, I. Tanaka, M. Nagao, R. Kanno, First-principles study on lithium removal from Li_2MnO_3, J. Power Sources 189 (2009) 798–801.
[7] S.H. Chen, Z.R. Xiao, P.H. Lee, Y.P. Liu, Y.K. Wang, Stability of half-metallic antiferromagnet La_2VMnO_6, first-principles calculation study, Phys. B Condens. Matter 406 (2011) 2783–2787.
[8] P. Yan, L. Xiao, J. Zheng, Y. Zhou, Y. He, X. Zu, S.X. Mao, J. Xiao, F. Gao, J.-G. Zhang, C.-M. Wang, Probing the degradation mechanism of Li_2MnO_3 cathode for Li-ion batteries, Chem. Mater. 27 (2015) 975–982.
[9] Y. Lyu, N. Zhao, E. Hu, R. Xiao, X. Yu, L. Gu, X.-Q. Yang, H. Li, Probing reversible multielectron transfer and structure evolution of $Li_{1.2}Cr_{0.4}Mn_{0.4}O_2$ cathode material for Li-ion batteries in a voltage range of 1.0–4.8 V, Chem. Mater. 27 (2015) 5238–5252.
[10] M. Sumita, Y. Tanaka, M. Ikeda, T. Ohno, Theoretically designed Li_3PO_4(100)/$LiFePO_4$(010) coherent electrolyte/cathode interface for all solid-state Li ion secondary batteries, J. Phys. Chem. C 119 (2015) 14–22.
[11] C. Ouyang, S. Shi, Z. Wang, X. Huang, L. Chen, First-principles study of Li ion diffusion in $LiFePO_4$, Phys. Rev. B 69 (2004).
[12] S. Shi, C. Ouyang, Z. Xiong, L. Liu, Z. Wang, H. Li, D.-s. Wang, L. Chen, X. Huang, First-principles investigation of the structural, magnetic, and electronic properties of olivine $LiFePO_4$, Phys. Rev. B 71 (2005).
[13] T. Maxisch, G. Ceder, Elastic properties of olivine Li_xFePO_4 from first principles, Phys. Rev. B 73 (2006).
[14] J.-M. Ateba Mba, C. Masquelier, E. Suard, L. Croguennec, Synthesis and crystallographic study of homeotypic $LiVPO_4F$ and $LiVPO_4O$, Chem. Mater. 24 (2012) 1223–1234.
[15] Y. Li, B. Huang, X. Cheng, Y. Zhang, Achieving high specific capacity through a two-electron reaction in hypothetical Li_2VFSiO_4: a first-principles investigation, J. Electrochem. Soc. 162 (2015) A787–A792.
[16] M.M. Islam, M. Wilkening, P. Heitjans, T. Bredow, Insights into Li(+) migration pathways in alpha-Li_3VF_6: a first-principles investigation, J. Phys. Chem. Lett. 3 (2012) 3120–3124.
[17] J. Barker, M.Y. Saidi, J.L. Swoyer, A comparative investigation of the Li insertion properties of the novel fluorophosphate phases, NaVPO[sub4]F and LiVPO [sub4]F, J. Electrochem. Soc. 151 (2004). A1670.
[18] J. Barker, M.Y. Saidi, J.L. Swoyer, Electrochemical insertion properties of the novel lithium vanadium fluorophosphate, LiVPO[sub4]F, J. Electrochem. Soc. 150 (2003). A1394.
[19] J. Barker, R.K.B. Gover, P. Burns, A. Bryan, M.Y. Saidi, J.L. Swoyer, Structural and electrochemical properties of lithium vanadium fluorophosphate, $LiVPO_4F$, J. Power Sources 146 (2005) 516–520.
[20] R. Gover, P. Burns, A. Bryan, M. Saidi, J. Swoyer, J. Barker, $LiVPO_4F$: a new active material for safe lithium-ion batteries, Solid State Ionics 177 (2006) 2635–2638.
[21] Y.U. Zhang, X. Bai, C. Li, Significant improvement of electrochemical performance of Cu-coated $LiVPO_4F$ cathode material for lithium-ion batteries, J. Chem. Sci. 127 (2015) 1411–1416.
[22] H. Yan, X. Wu, Y. Li, Preparation and characterization of conducting polyaniline-coated $LiVPO_4F$ nanocrystals with core-shell structure and its application in lithium-ion batteries, Electrochim. Acta 182 (2015) 437–444.
[23] J.-x. Wang, Z.-x. Wang, L. Shen, X.-h. Li, H.-j. Guo, W.-j. Tang, Z.-g. Zhu, Synthesis and performance of $LiVPO_4F$/C-based cathode material for lithium ion battery, Trans. Nonferrous Metals Soc. China 23 (2013) 1718–1722.
[24] J.-q. Liu, S.-k. Zhong, L. Wu, K. Wan, F. LÜ, Electrochemical performance of $LiVPO_4F$/C synthesized by different methods, Trans. Nonferrous Metals Soc. China 22 (2012) s157–s161.
[25] B. Zhang, Y.-d. Han, J.-c. Zheng, C. Shen, L. Ming, J.-f. Zhang, A novel lithium vanadium fluorophosphate nanosheet with uniform carbon coating as a cathode material for lithium-ion batteries, J. Power Sources 264 (2014) 123–127.
[26] Z. Xiong, G. Zhang, J. Xiong, X. Yang, Y. Zhang, Modified sol–gel synthesis of nanosized $LiVPO_4F$/C cathode material with mechanical blending assist, Mater. Lett. 111 (2013) 214–216.
[27] J. Wang, X. Li, Z. Wang, H. Guo, Y. Zhang, X. Xiong, Z. He, Synthesis and characterization of $LiVPO_4F$/C using precursor obtained through a soft chemical route with mechanical activation assist, Electrochim. Acta 91 (2013) 75–81.
[28] Z. Liu, W. Peng, Y. Fan, X. Li, Z. Wang, H. Guo, J. Wang, A new route for graphene wrapping $LiVPO_4F$/C nano composite toward superior lithium storage property, J. Alloys Compd. 639 (2015) 496–503.
[29] J. Wang, X. Li, Z. Wang, B. Huang, Z. Wang, H. Guo, Nanosized $LiVPO_4F$/graphene composite: a promising anode material for lithium ion batteries, J. Power Sources 251 (2014) 325–330.
[30] Z. Liu, W. Peng, Y. Fan, X. Li, Z. Wang, H. Guo, J. Wang, One-step facile synthesis of graphene-decorated $LiVPO_4F$/C nanocomposite as cathode for high-performance lithium ion battery, Ceram. Int. 41 (2015) 9188–9192.
[31] P. Zhang, D. Zhang, L. Huang, Q. Wei, M. Lin, X. Ren, First-principles study on the electronic structure of a $LiFePO_4$ (010) surface adsorbed with carbon, J. Alloys Compd. 540 (2012) 121–126.
[32] Xiaofang Ouyang, Molin Lei, Siqi Shi, Cuilan Luo, Desheng Liu, Diyou Jiang, Zhiqing Ye, Minsheng Lei, First-principles studies on surface electronic structure and stability of $LiFePO_4$, J. Alloys Compd. 476 (2009) 462–465.
[33] L. Wang, F. Zhou, Y.S. Meng, G. Ceder, First-principles study of surface properties of $LiFePO_4$: surface energy, structure, Wulff shape, and surface redox potential, Phys. Rev. B 76 (2007).
[34] Y.H. Lee, X.Q. Zhang, W. Zhang, M.T. Chang, C.T. Lin, K.D. Chang, Y.C. Yu, J.T. Wang, C.S. Chang, L.J. Li, T.W. Lin, Synthesis of large-area MoS_2 atomic layers with chemical vapor deposition, Adv. Mater. 24 (2012) 2320–2325.
[35] K.K. Liu, W. Zhang, Y.H. Lee, Y.C. Lin, M.T. Chang, C.Y. Su, C.S. Chang, H. Li, Y. Shi, H. Zhang, C.S. Lai, L.J. Li, Growth of large-area and highly crystalline MoS_2 thin layers on insulating substrates, Nano Lett. 12 (2012) 1538–1544.
[36] D. Kong, H. Wang, J.J. Cha, M. Pasta, K.J. Koski, J. Yao, Y. Cui, Synthesis of MoS_2

and $MoSe_2$ films with vertically aligned layers, Nano Lett. 13 (2013) 1341–1347.
[37] C. Ataca, M. Topsakal, E. Aktürk, S. Ciraci, A comparative study of lattice dynamics of three- and two-dimensional MoS_2, J. Phys. Chem. C 115 (2011) 16354–16361.
[38] V.P. Santos, B. van der Linden, A. Chojecki, G. Budroni, S. Corthals, H. Shibata, G.R. Meima, F. Kapteijn, M. Makkee, J. Gascon, Mechanistic insight into the synthesis of higher alcohols from syngas: the role of K promotion on MoS_2 catalysts, ACS Catal. 3 (2013) 1634–1637.
[39] H. Li, J. Wu, Z. Yin, H. Zhang, Preparation and applications of mechanically exfoliated single-layer and multilayer MoS(2) and WSe(2) nanosheets, Acc. Chem. Res. 47 (2014) 1067–1075.
[40] Y. Guo, D. Liu, J. Robertson, 3D behavior of schottky barriers of 2D transition-metal dichalcogenides, ACS Appl. Mater. Interfaces 7 (2015) 25709–25715.
[41] K. Kalantar-zadeh, J.Z. Ou, Biosensors based on two-dimensional MoS_2, ACS Sens. 1 (1) (2016) 5–16.
[42] John P. Perdew, Kieron Burke, Matthias Ernzerhof, Generalized gradient approximation made simple, Phys. Rev. Lett. 77 (1996) 3865–3868.
[43] G. Kresse, Efficient iterative schemes for ab initio total-energy calculations using a plane-wave basis set, Phys. Rev. B 54 (1996) 169–186.
[44] R.C. Kari Laasonen, Changyol Lee, David Vanderbilt, Implementation of ultrasoft pseudo potentials in ab initio molecular dynamics, Phys. Rev. B 43 (1991), 6796.
[45] H.J. Monkhorst, J.D. Pack, Special points for Brillouin-zone integrations, Phys. Rev. B 13 (1976), 5188.
[46] S.H. Chen, Z.R. Xiao, Y.P. Liu, P.H. Lee, Y.K. Wang, First-principle calculation on nearly half-metallic antiferromagnetic behavior of double perovskites La_2VReO_6, J. Magn. Magn. Mater. 323 (2011) 175–178.
[47] C.J. O'Brien, Z. Rák, D.W. Brenner, Calculated stability and structure of nickel ferrite crystal surfaces in hydrothermal environments, J. Phys. Chem. C 118 (2014) 5414–5423.
[48] J.L. Nie, H.Y. Xiao, F. Gao, X.T. Zu, Electronic and magnetic properties of Al adsorption on α-uranium (001) surface: Ab initio calculations, J. Alloys Compd. 476 (2009) 675–682.
[49] X. Lv, Z. Xu, J. Li, J. Chen, Q. Liu, Investigation of fluorine adsorption on nitrogen doped $MgAl_2O_4$ surface by first-principles, Appl. Surf. Sci. (2016) 97–104.
[50] C.M.F.N.J. van der Laag, G. de With, Geometry of {001} surfaces of spinel ($MgAl_2O_4$): first-principles simulations and experimental measurements, J. Am. Ceram. Soc. 88 (2005) 1544–1548.
[51] S.W. Oh, S.T. Myung, S.M. Oh, K.H. Oh, K. Amine, B. Scrosati, Y.K. Sun, Double carbon coating of $LiFePO_4$ as high rate electrode for rechargeable lithium batteries, Adv. Mater. 22 (2010) 4842–4845.
[52] Y. Wu, Z. Wen, J. Li, Hierarchical carbon-coated $LiFePO_4$ nanoplate microspheres with high electrochemical performance for Li-ion batteries, Adv. Mater. 23 (2011) 1126–1129.
[53] B. Wang, D. Wang, Q. Wang, T. Liu, C. Guo, X. Zhao, Improvement of the electrochemical performance of carbon-coated $LiFePO_4$ modified with reduced graphene oxide, J. Mater. Chem. A 1 (2013) 135–144.
[54] C.M. Julien, K. Zaghib, A. Mauger, M. Massot, A. Ait-Salah, M. Selmane, F. Gendron, Characterization of the carbon coating onto LiFePO[sub4] particles used in lithium batteries, J. Appl. Phys. 100 (2006), 063511.
[55] J.D. Wilcox, M.M. Doeff, M. Marcinek, R. Kostecki, Factors influencing the quality of carbon coatings on LiFePO[sub4], J. Electrochem. Soc. 154 (2007). A389.
[56] F. Brochu, A. Guerfi, J. Trottier, M. Kopeć, A. Mauger, H. Groult, C.M. Julien, K. Zaghib, Structure and electrochemistry of scaling nano C–$LiFePO_4$ synthesized by hydrothermal route: complexing agent effect, J. Power Sources 214 (2012) 1–6.
[57] F. Pan, W.-l. Wang, H. Li, X. Xin, Q. Chang, W. Yan, D. Chen, Investigation on a core–shell nano-structural $LiFePO_4$/C and its interfacial CO interaction, Electrochim. Acta 56 (2011) 6940–6944.
[58] K. Yang, Z. Deng, J. Suo, Synthesis and characterization of $LiFePO_4$ and $LiFePO_4$/C cathode material from lithium carboxylic acid and Fe^{3+}, J. Power Sources 201 (2012) 274–279.